Where photons meet phonons

Buters, F.M.

2

Theory and Experimentals

In this chapter we present a derivation of the optomechanical equations of motions and connect these to observable quantities. In the second part of this chapter a brief overview of the experimental set-up and methods is presented. Both the theory and experimental details form the basis for the following chapters.

2.1 Optomechanical equations of motion

Although the field of cavity optomechanics contains a wide variety of optical and microwave cavities coupled to an assortment of mechanical oscillators (see Ref. [16] for an overview), most systems can be represented by the schematic picture in Fig. 2.1. In such a Fabry-Perot cavity, the displacement of the mirror is parametrically[1] coupled to the cavity field, leading to intricate dynamics. Since most of the work presented in this thesis is classical, we will derive the semi-classical equations of motions because these provide a more intuitive understanding of the physics involved. The approach presented here is inspired by the work of Schliesser [17] and Rivière [18]. A more detailed Hamiltonian description is presented in the work of Law [19] and a quantum mechanical treatment can be found in the works of Marquardt [20] and Wilson-Rae [21].

2.1.1 Uncoupled equations

As can be seen from Fig. 2.1, the two main ingredients are a harmonic oscillator and an optical cavity. First we consider the harmonic oscillator and cavity separately. The motion of the harmonic oscillator is described by the following differential equation:

$$\frac{d^2x(t)}{dt^2} = -\Gamma_m \frac{dx(t)}{dt} - \Omega_m^2 x(t) + \frac{F_{ex}}{m} \tag{2.1}$$

[1] A parametric oscillator is an oscillator of which one parameter varies with time. In an optomechanical system, the cavity field varies with the frequency of the mechanical resonator, leading to a resonant optical force.

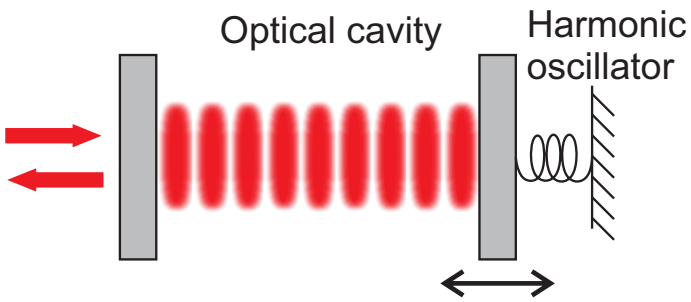

Figure 2.1: Schematic overview of an optomechanical system. In a Fabry-Perot cavity with one moving end mirror the motion of the harmonic oscillator is parametrically coupled to the cavity field.

where we have defined the mechanical displacement $x(t)$, the mechanical damping rate Γ_m, the mechanical frequency Ω_m, the mode mass m and some external force F_{ex}.

Eq. (2.1) can be solved easily by introducing the Fourier transform $x(\omega) = \int_{-\infty}^{\infty} x(t)e^{i\omega t}\,\mathrm{d}t$. The solution can then be written as $x(\omega) = \chi_{xx}F_{ex}(\omega)$ where χ_{xx} is the mechanical susceptibility defined as:

$$\chi_{xx}(\omega) = (m(\Omega_m^2 - \omega^2) - im\Gamma_m\omega)^{-1}. \tag{2.2}$$

When Γ_m is small, this equation is well described by a Lorentzian: $\chi_{xx}(\omega) = (m\Omega_m[2(\Omega_m - \omega) - i\Gamma_m])^{-1}$.

A Fabry-Perot cavity is typically described in terms of the circulating electrical field E_{circ}: [22][2]

$$E_{circ} = t_1 E_{inc} + r_1 r_2 e^{-2i\phi} E_{circ} \tag{2.3}$$

where E_{inc} is the incoming electrical field, t_1 the amplitude transmission coefficient of the entrance mirror, r_1 and r_2 the amplitude reflection coefficient of both mirrors and ϕ the phase acquired after one round-trip through the cavity. This equation is useful to describe the steady state of an optical cavity. However, we are interested in the dynamics of the circulating intensity inside the cavity, as will become clear in the next section. It is therefore useful to describe the field inside the optical cavity in terms of a complex mode amplitude $\alpha(t)$ which is normalized such that $|\alpha(t)|^2$ is the photon number or stored energy [23]:

$$\frac{d\alpha(t)}{dt} = -\frac{\kappa}{2}\alpha(t) - i\omega_{cav}\alpha(t) + \sqrt{\kappa_{ex}}\sigma_{in}(t) \tag{2.4}$$

where we have defined the optical decay rate κ, the cavity frequency ω_{cav}, the external optical coupling rate κ_{ex} and the optical input power σ_{in}. An elegant classical

[2]Equation (2.3) describes only the magnitude of the circulating electrical field. The spatial profile can be described using Hermite-Gaussian modes. In this thesis only the fundamental Hermite-Gaussian mode is used.

derivation of this equation using an LC-circuit as an example is provided by Haus [23] while a quantum treatment is given by Gardiner and Collet [24].

To solve Eq. (2.4), it is convenient to choose a coordinate frame rotating with the laser frequency ω_L by defining $\alpha(t) = a(t)e^{-i\omega_L t}$ and $\sigma_{in}(t) = s_{in}(t)e^{-i\omega_L t}$. This yield the following equation:

$$\frac{da(t)}{dt} = (i\Delta - \frac{\kappa}{2})a(t) + \sqrt{\kappa_{ex}}s_{in}(t) \tag{2.5}$$

where the laser detuning Δ is introduced as the difference between laser and cavity frequency, $\Delta = \omega_L - \omega_{cav}$. Typically negative or red detuning is used to indicate a laser with a frequency lower than the cavity resonance ($\Delta < 0$) and positive or blue detuning for the case where the laser frequency is higher than the cavity resonance ($\Delta > 0$).[3] The steady state solution to Eq. (2.5) is obtained by assuming a constant input mode amplitude $s_{in}(t)$ and setting $da(t)/dt$ to zero, resulting in a mean mode amplitude of:

$$\bar{a} = \frac{\sqrt{\kappa_{ex}}s_{in}}{-i\Delta + \kappa/2}. \tag{2.6}$$

2.1.2 Optomechanical interaction

With the terminology in place, we can turn our attention to the optomechanical interaction itself. In particular, we will show how the coupling between the mechanical motion and the cavity field modifies the response of both the harmonic oscillator (Eq. (2.2)) and the mode amplitude (Eq. (2.6)). The parametric coupling of the mechanical motion to the cavity mode modulates the cavity resonance frequency:

$$\omega_{cav}(x) = \omega_{cav} + x\partial\omega_{cav}/\partial x \tag{2.7}$$

where we have assumed the mechanical motion to be small, such that this linear approximation holds. The expression can be simplified by introducing the optical frequency per displacement as $G = -\partial\omega_{cav}/\partial x$. The typical convention is to define G in such a way that for $x > 0$ the cavity length increases, leading to a decrease in ω_{cav}, hence the minus sign. For a Fabry-Perot cavity as depicted in Fig. 2.1, $G = \omega_{cav}/L$ with L the cavity length. Due to the displacement of the mirror, the cavity resonance frequency changes as $Gx(t)$. Therefore the optomechanical equation for the cavity mode is:

$$\frac{da(t)}{dt} = \left[i(\Delta + Gx(t)) - \frac{\kappa}{2}\right] a(t) + \sqrt{\kappa_{ex}}s_{in}(t). \tag{2.8}$$

The radiation pressure arises from the momentum transfer when a photon reflects off the moving mirror. The radiation pressure is therefore proportional to the number of circulating photons $|a(t)|^2$ and to twice the photon momentum $\hbar k$, with $k = \omega_{cav}/c$ the wave vector. Finally, the photon round-trip time, $c/2L$ with c the

[3] A small warning: In literature the definition of detuning can vary from article to article. In this thesis terminology and definitions are chosen to be consistent with the work of Aspelmeyer et al. [16]

speed of light, needs to be taken into account. The radiation pressure force is therefore:

$$\begin{aligned} F_{rad} &= \frac{\Delta p}{\Delta t} \\ &= |a(t)|^2 \frac{c}{2L} 2\hbar k = \hbar G |a(t)|^2 \end{aligned} \tag{2.9}$$

where $G = \omega_{cav}/L$ is used to simplify the expression. The equation of motion of the harmonic oscillator becomes:

$$\frac{d^2x(t)}{dt^2} = -\Gamma_m \frac{dx(t)}{dt} - \Omega_m^2 x(t) + \frac{\hbar G}{m}|a(t)|^2 + \frac{F_{ex}}{m}. \tag{2.10}$$

Equations (2.8) and (2.10) form the theoretical basis of the work presented in this thesis. These coupled non-linear equations are difficult to solve. However, with appropriate assumptions, analytic solutions can still be found. For example, the motion of the harmonic oscillator can be treated as a small perturbation around some mean displacement: $x(t) = \bar{x} + \delta x(t)$. Similarly, the effect of this motion on the cavity field can be treated as a perturbation: $a(t) = \bar{a} + \delta a(t)$. Substituting these assumptions in Eqs. (2.8) and (2.10) yields:

$$\frac{d\delta a(t)}{dt} = (i[\Delta + G(\bar{x} + \delta x(t))] - \frac{\kappa}{2})(\bar{a} + \delta a(t)) + \sqrt{\kappa_{ex}} s_{in} \tag{2.11}$$

$$\frac{d^2\delta x(t)}{dt^2} = -\Gamma_m \frac{d\delta x(t)}{dt} - \Omega_m^2(\bar{x} + \delta x(t)) + \frac{\hbar G}{m}[(\bar{a} + \delta a(t))(\bar{a}^* + \delta a^*(t))] + \frac{F_{ex}}{m} \tag{2.12}$$

As with the uncoupled case, a steady state solution can be found by setting $\delta a(t) = 0$ and $\delta x(t) = 0$:

$$\bar{a} = \frac{\sqrt{\kappa_{ex}} s_{in}}{i(\Delta + G\bar{x}) - \kappa/2} \tag{2.13}$$

$$\bar{x} = \frac{\hbar G}{m\Omega_m^2}|\bar{a}|^2. \tag{2.14}$$

Already the steady-state solution shows an interesting effect: the mean photon number in the cavity depends on the mean displacement. However, the mean photon number also causes a static radiation pressure force on the mirror, thus changing the cavity resonance frequency. This in turn influences the mean photon number. Solving Eqs. (2.13) and (2.14) yields a cubic expression for $\bar{a}$ with stable and unstable solutions [25].

We can also solve for $\delta a(t)$ and $\delta x(t)$. Using Eqs. (2.13) and (2.14), dropping second-order terms and introducing $\tilde{\Delta} = \Delta + G\bar{x}$ one obtains:[4]

$$\frac{d\delta a(t)}{dt} = \left[i\tilde{\Delta} - \frac{\kappa}{2}\right] \delta a(t) + iG\bar{a}\delta x(t) \tag{2.15}$$

[4]Note that we have also used $\bar{a} = \bar{a}^*$. This is valid since the phase of $\bar{a}$, which follows from the phase of the incoming beam, can always be set to zero.

$$\frac{d^2\delta x(t)}{dt^2} = -\Gamma_m \frac{d\delta x(t)}{dt} - \Omega_m^2 \delta x(t) + \frac{\hbar G\bar{a}}{m}[\delta a(t) + \delta a^*(t)] + \frac{F_{ex}}{m}. \tag{2.16}$$

As for the uncoupled equations, this is best solved by applying the Fourier transform. Besides taking the Fourier transform of the equations above, it is convenient to also write down the Fourier transform of the complex conjugate of Eq. (2.15) to obtain the following three equations:[5]

$$-i\omega\delta a(\omega) = (i\tilde{\Delta} - \frac{\kappa}{2})\delta a(\omega) + iG\bar{a}\delta x(\omega) \tag{2.17}$$

$$-i\omega\delta a^*(\omega) = (-i\tilde{\Delta} - \frac{\kappa}{2})\delta a^*(\omega) - iG\bar{a}\delta x(\omega) \tag{2.18}$$

$$-\omega^2\delta x(\omega) = +i\omega\Gamma_m\delta x(\omega) - \Omega_m^2\delta x(\omega) + \frac{\hbar G\bar{a}}{m}[\delta a(\omega) + \delta a^*(\omega)] + \frac{F_{ex}(\omega)}{m}. \tag{2.19}$$

Solving Eqs. (2.17) - (2.18) gives:

$$\delta a(\omega) = \frac{iG\bar{a}\delta x(\omega)}{\kappa/2 - i(\tilde{\Delta} + \omega)} \tag{2.20}$$

$$\delta a^*(\omega) = \frac{-iG\bar{a}\delta x(\omega)}{\kappa/2 + i(\tilde{\Delta} - \omega)} \tag{2.21}$$

which can readily be used to derive an expression for the radiation pressure force

$$\begin{aligned}
\delta F_{rad}(\omega) &= \hbar G\bar{a}(\delta a(\omega) + \delta a^*(\omega)) \\
&= -\hbar G^2\bar{a}^2\left(\frac{\tilde{\Delta}+\omega}{\kappa^2/4 + (\tilde{\Delta}+\omega)^2} + \frac{\tilde{\Delta}-\omega}{\kappa^2/4 + (\tilde{\Delta}-\omega)^2}\right)\delta x(\omega) \\
&+ i\hbar G^2\bar{a}^2\left(\frac{\kappa/2}{\kappa^2/4 + (\tilde{\Delta}+\omega)^2} - \frac{\kappa/2}{\kappa^2/4 + (\tilde{\Delta}-\omega)^2}\right)\delta x(\omega).
\end{aligned} \tag{2.22}$$

In the Fourier domain, the radiation pressure has both a real and imaginary component. The real component results in an optical spring effect, while the imaginary component generates an optical damping force. This can be shown explicitly by inserting the result of Eq. (2.22) back in Eq. (2.19). As for the uncoupled case, the solution can be written as $x(\omega) = \chi_{\mathit{eff}}(\omega)F_{ex}(\omega)$ with $\chi_{\mathit{eff}}(\omega)$ the effective susceptibility:

$$\chi_{\mathit{eff}}(\omega) = \left[m(\Omega_m^2 + \frac{k_{opt}(\omega)}{m} - \omega^2)\right] - im\omega\left[\Gamma_m + \Gamma_{opt}(\omega)\right]^{-1}. \tag{2.23}$$

in which the optical spring constant $k_{opt}(\omega)$ and optical damping $\Gamma_{opt}(\omega)$ are defined as:

$$k_{opt}(\omega) = \frac{\hbar G^2\bar{a}^2}{m}\left(\frac{\tilde{\Delta}+\omega}{\kappa^2/4 + (\tilde{\Delta}+\omega)^2} + \frac{\tilde{\Delta}-\omega}{\kappa^2/4 + (\tilde{\Delta}-\omega)^2}\right). \tag{2.24}$$

[5] Again we have used the freedom to set the phase in such a way that δx is real.

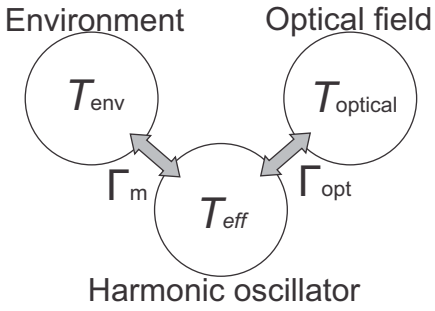

Figure 2.2: The harmonic oscillator is coupled to the environment with coupling rate Γ_m and to the optical field with coupling rate Γ_{opt}.

$$\Gamma_{opt}(\omega) = \frac{\hbar G^2 \bar{a}^2}{m\omega}\left(\frac{\kappa/2}{\kappa^2/4+(\tilde{\Delta}+\omega)^2} - \frac{\kappa/2}{\kappa^2/4+(\tilde{\Delta}-\omega)^2}\right) \tag{2.25}$$

Finally, when the optical spring effect and optical damping are small, the effective resonance frequency and effective damping rate are given by:[6]

$$\Omega_{\mathit{eff}} = \Omega_m + g^2\left(\frac{\Delta+\Omega_m}{\kappa^2/4+(\Delta+\Omega_m)^2} + \frac{\Delta-\Omega_m}{\kappa^2/4+(\Delta-\Omega_m)^2}\right) \tag{2.26}$$

$$\Gamma_{\mathit{eff}} = \Gamma_m + g^2\left(\frac{\kappa}{\kappa^2/4+(\Delta+\Omega_m)^2} - \frac{\kappa}{\kappa^2/4+(\Delta-\Omega_m)^2}\right) \tag{2.27}$$

where the multi-photon coupling rate g, defined as $g^2 = \frac{\hbar G^2 \bar{a}^2}{2m\Omega_m}$ is introduced, and the static radiation pressure is assumed to be small such that $\tilde{\Delta} \approx \Delta$.

Comparing the uncoupled case with the case including optomechanical interaction, one sees that the motion of the harmonic oscillator creates a radiation pressure force which, when acting back on the mirror, modifies the resonance frequency and damping rate. The magnitude of this effect, not surprisingly, varies with input laser power. More importantly, however, for specific laser detunings the radiation pressure causes predominantly an optical spring effect or an optical damping. Furthermore, for positive detunings, anti-damping can occur, leading to a reduction of the effective damping rate and even driving of the mechanical motion. This phenomena is explored in detail in chapter 3.

So far we have only discussed the modifications to the mechanical response. The optical damping however couples the harmonic oscillator to the laser bath. In the next section the consequence, namely optical cooling, will be discussed together with methods to measure this effect.

2.1.3 Optical cooling

When deriving the response for the harmonic oscillator in the presence of an optical field, Γ_m has only been thought of as a damping rate. However, it also couples the

[6]The Taylor approximation $\Omega_{\mathit{eff}} = \sqrt{\Omega_m^2 + \frac{k_{opt}(\omega)}{m}} \approx \Omega_m + k_{opt}/2m\Omega_m$ is used.

oscillator to the environment which is at some temperature T_{env}. The fluctuation-dissipation theorem describes the thermodynamics of such coupled systems [26, 27, 28]. Coupling to a thermal environment (or thermal bath) generates a force which acts on the oscillator in such a way that, when in equilibrium, the variance of the displacement is proportional to the environmental temperature T_{env}:

$$\left.\begin{aligned} E &= \frac{1}{2} m\Omega_m^2 \langle x(t)^2 \rangle \\ E &= \frac{1}{2} k_b T_{env} \end{aligned}\right\} \qquad \langle x(t)^2 \rangle = \frac{k_b T_{env}}{m\Omega_m^2} \tag{2.28}$$

which is the equipartition theorem. In other words: the displacement of a harmonic oscillator coupled to a thermal bath is such that the mode temperature is equal to the bath temperature. When now the coupling with the cavity field is included, we have the situation as depicted in Fig. 2.2. The harmonic oscillator is coupled with coupling rate Γ_m to a bath at temperature T_{env}, and coupled with coupling rate Γ_{opt} to the optical field. By assuming thermal equilibrium, the effective temperature of the harmonic oscillator can therefore be written as:

$$T_{\mathit{eff}} = \frac{T_{env}\Gamma_m + T_{optical}\Gamma_{opt}}{\Gamma_{opt} + \Gamma_m}. \tag{2.29}$$

Although it might be strange to label a coherent optical field with a temperature, from a noise perspective, a coherent optical field has an effective temperature of zero [29]. With this, Eq. 2.29 reduces to

$$T_{\mathit{eff}} = T_{env}\frac{\Gamma_m}{\Gamma_{opt} + \Gamma_m}. \tag{2.30}$$

Note that at sufficiently low effective temperatures, this equation no longer holds and one has to take the photon shot noise into account as well. For the results presented in this thesis, the effective temperature is still high enough for Eq. (2.30) to be valid. With the full quantum theory, one can also show that optical cooling to the quantum mechanical ground state is possible when $\kappa \ll \Omega_m$[7]. This limit is often referred to as the side-band resolved limit. Most of the experiments presented in this thesis operate in the side-band resolved limit.

One can obtain the effective mode temperature by recording $x(t)$, determining the variance and using the equipartition theorem. A more elegant way would be to record $x(t)$ and take the Fourier transform to obtain the power spectral density (PSD) S_{xx}, because the fluctuation-dissipation theorem relates S_{xx} to the effective temperature by:

$$S_{xx}(\omega) = 2\frac{k_b T_{\mathit{eff}}}{\omega}\mathrm{Im}\chi_{\mathit{eff}}(\omega). \tag{2.31}$$

[7]The requirement of $\kappa \ll \Omega_m$ only applies when optical side-band cooling is used as the cooling method. Active feedback cooling [30] and so called "dissipative" optomechanical coupling [31] do not require to be side-band resolved. So far, however, only side-band cooling has successfully been used to reach the quantum mechanical ground-state.

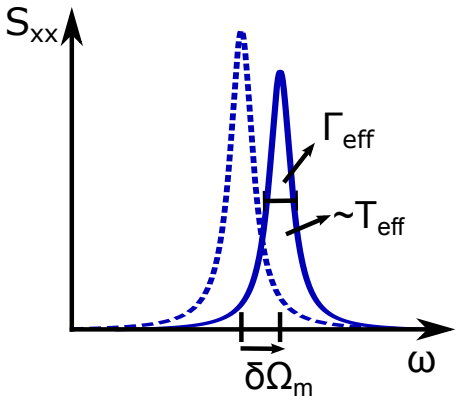

Figure 2.3: A measurement of the power spectral density of the mechanical motion gives directly the parameters of interest, namely the effective temperature, mechanical linewidth and resonance frequency.

Integrating S_{xx} over all frequencies, results in the following:

$$\begin{aligned} \int_{-\infty}^{\infty} S_{xx}(\omega)\,\frac{\mathrm{d}\omega}{2\pi} &= \frac{k_b T_{\mathit{eff}}}{m\Omega_m^2} \\ &= \langle x(t)^2 \rangle \end{aligned} \tag{2.32}$$

where Eq. (10.4) was used in the last line.

Not only does integrating the mechanical PSD directly give the effective temperature, but the Lorentzian resonance also gives the effective linewidth and frequency shift, as is shown in Fig. 2.3. Therefore, the full optomechanical interaction is characterized by measuring the PSD of the mechanical motion. But how to measure $x(t)$ to obtain the mechanical PSD?

We have already seen that due to the movement of the mirror, the cavity resonance frequency changes according to $Gx(t)$. Therefore, any change in cavity resonance frequency is directly proportional to the displacement. There are two methods for measuring changes in the cavity resonance frequency. In Fig. 2.4(a) the side-of-fringe method is shown. By placing a laser to the side of the cavity resonance, a small change in cavity length leads to a change in mode amplitude which can be measured by monitoring the transmitted intensity. The resulting signal can also be used to keep a laser locked to a certain frequency with respect to the cavity resonance (side-of-fringe lock).

The other method is a phase sensitive detection method, as is shown in Fig. 2.4(b). This method is actually preferred, because the read-out can take place exactly at the cavity resonance, which is not possible with the side-of-fringe method. Since there is no optomechanical effect at zero detuning, the motion of the resonator can be obtained without influencing the system.[8] Finally, the phase sensitive method is, to first order, not sensitive to laser intensity fluctuations.

[8]Here we consider only the classical case. In the quantum description, the photon shot noise sets

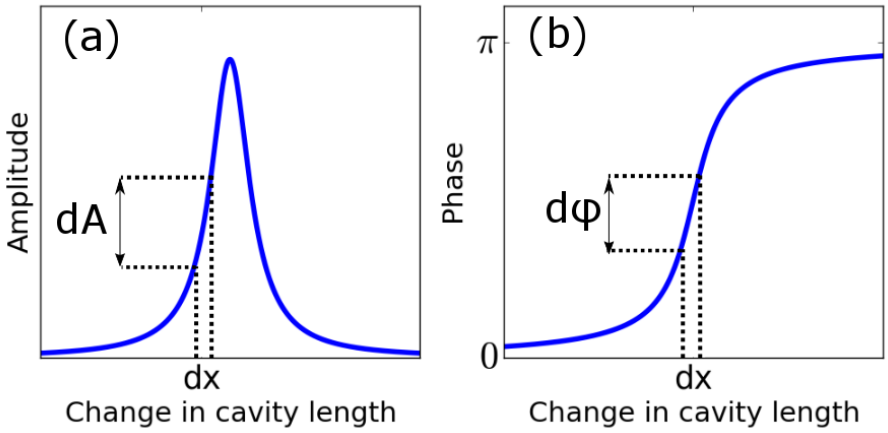

Figure 2.4: Amplitude (a) and phase response (b) of an optical resonance. The mirror displacement can be measured in two ways: side-of-fringe method as shown in (a) and via a phase sensitive detection method shown in (b).

2.2 Experimentals

With the basics of the optomechanical interaction discussed, such as optical cooling and displacement transduction, we turn to the experimental aspects of this thesis. First, the "optical bench" containing the cavity and trampoline resonator is briefly described, before continuing with an overview of the trampoline resonator. Finally, we introduce the core of the experimental methods used in this thesis, including the laser scheme.

2.2.1 Optical bench

The optical bench, designed by H. van der Meer, has a compact footprint such that integration in a cryogenic system is possible. The bench is made from brass and constructed around a 5 cm long optical cavity. A length of 5 cm was chosen as a compromise between optical path length and mirror quality. A larger cavity length would benefit the superposition schemes mentioned in the introductory chapter. However, a longer cavity requires larger mirrors, which are more difficult to fabricate.

In Fig. 2.5(a) a schematic overview of the bench is shown. The light enters the system via an optical fiber (Nufern 1060-XP) after which it is collimated using an aspheric lens (Edmund Optics 15 mm diameter 22.5 mm EFL). Via a periscope consisting of two adjustable mirrors the light passes through a mode-matching lens (Thorlabs Best Form LBF254-050-C) and enters the cavity through a 1/2 inch superpolished mirror with a 5 cm radius of curvature (Advanced Thin Films and Laser Optik). After passing through the trampoline resonator, the transmitted signal is col-

a lower limit to the measurement precision, leading to the formulation of the standard quantum limit (SQL).

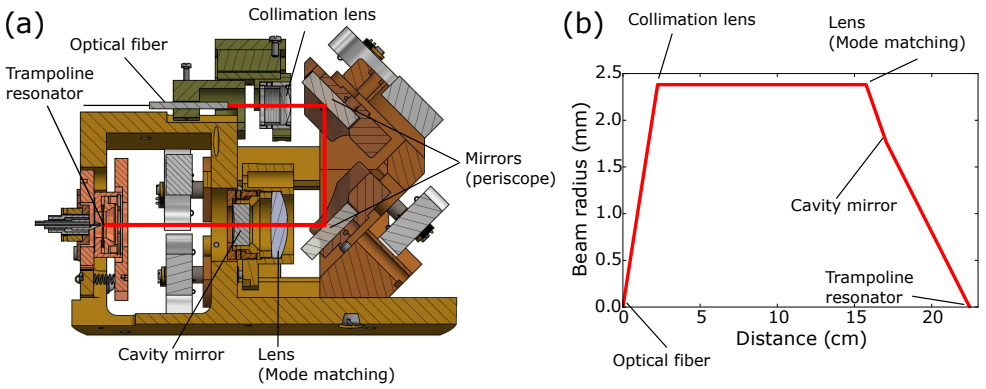

Figure 2.5: (a) Schematic overview of the optical bench with the key components indicated. (b) Beam radius as function of propagation distance along the optical path represented by the red line in (a) calculated using Gaussian beam optics.

lected via a photo-detector (Hamamatsu G10899-005K, connected to a Femto DHPCA-100 amplifier) placed behind the cavity. The reflected light is collected by the fiber that also brings the light to the set-up. The optical components are chosen to ensure optimal mode-matching to the fundamental cavity mode by using Gaussian beam theory and ray matrices [32]. The resulting beam radius as function of propagation distance is shown in Fig. 2.5(b).

The cavity alignment is quite sensitive, requiring sub-micron adjustments. Therefore, the collimation lens is placed on an Attocube translation stage and both the large cavity mirror and periscope mirrors are adjustable by Piezoknobs from JPE. These cryogenic compatible actuators also ensure that the alignment is adjustable to compensate for the inevitable contraction that occurs when cooling down the set-up.

The entire set-up is placed in a vacuum chamber with passive vibration isolation involving a damped mass-spring system to decouple the set-up from any environmental disturbances. For the cryogenic experiments in a cryogen-free cryostat, a more elaborate vibration isolation stage is developed, which we will discuss in more detail in chapter 10. All experiments discussed in this thesis are performed in medium to high vacuum (typically $<1\times10^{-3}$ mbar) to eliminate the effect of gas damping on the mechanical properties of the trampoline resonator.

2.2.2 Trampoline resonators

The trampoline resonators used throughout this thesis are fabricated by colleagues at UCSB (B. Pepper, M. Weaver and F. Luna). Here we will highlight the important fabrication steps of these trampoline resonators, the precise details can be found elsewhere [33, 34].

High stress silicon nitride (typically 850 MPa) is deposited on a super-polished silicon wafer. Next, a distributed Bragg reflector (DBR) of alternating layers of Ta_2O_5 and SiO_2 is deposited by Advanced Thin Films and in later stages of this work by Laser Optik. A DBR mirror is the only way to achieve the reflectivity ($R > 0.99997$)

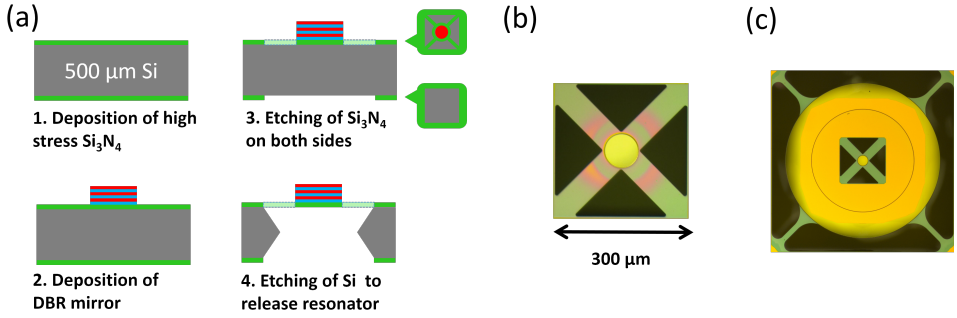

Figure 2.6: (a) The four main fabrication steps to make a trampoline resonator. (b) Optical microscope image of the trampoline resonator. (c) Optical microscope image of a nested trampoline resonator.

we need to create a high quality cavity. Using lithography and etching, the silicon nitride is patterned to achieve the desired resonator design. Finally the silicon is etched away to release the resonator. These steps are schematically indicated in Fig. 2.6(a) together with an optical microscope image of the finished resonator in Fig. 2.6(b). Typically the mirror has a diameter between 60 and 130 μm, while the frequency of the resonator lies between 150 and 350 kHz, with a mode-mass between 100 and 500 ng.

The design with four arms, as shown in Fig. 2.6(b), ensures that higher order mechanical modes have a much higher frequencies than the fundamental mechanical mode and couple poorly to the cavity field. The only mechanical mode that is therefore considered in this thesis is the fundamental out-of-plane mode of the trampoline resonator.

Besides a single resonator, also a nested resonator [35], as shown in Fig. 2.6(c), was used in parts of this thesis. In chapter 7, we will come back to the necessity for this modified design. The fabrication process of the nested resonator is essentially the same as depicted in Fig. 2.6(a).

2.2.3 Aligning the optical bench

The alignment of the optical bench shown in Fig. 2.5(a) has two parts: the coupling to the cavity mode, and the alignment of the cavity itself. The coupling to the correct cavity mode is achieved by adjusting the periscope, together with the collimation lens. If the periscope is set incorrectly, higher order Hermite-Gaussian modes become visible as is shown in Fig. 2.7.

Because of the small mirror on the trampoline resonator, the cavity operates as a near-hemispherical resonator [22] with the beam waist close to the small mirror. As a consequence, the size of the cavity mode at the entrance mirror is quite large. The influence of cavity length on the beam radius[9] for both the large entrance mirror and the small mirror is shown in Fig. 2.8(a) and (b). When the cavity approaches

[9]The beam radius is defined as the radius at which the intensity drops by $1/e^2$

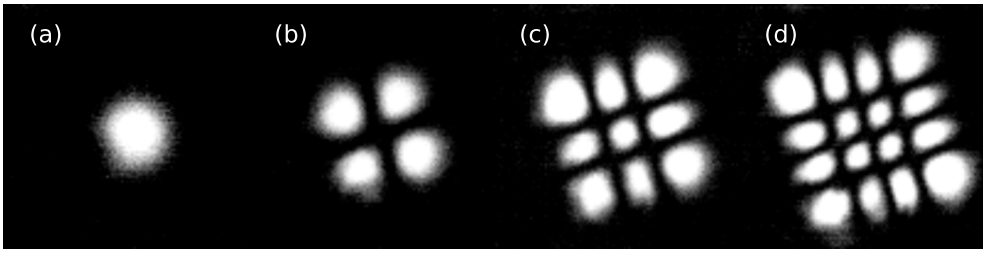

Figure 2.7: Different Hermite-Gaussian modes exist in the optical cavity, depending on the settings of the periscope. (a) The fundamental mode (TEM_{00}) considered here in this thesis. Examples of other possible modes are: (b) TEM_{11} mode (c) TEM_{22} and (d) TEM_{33} mode.

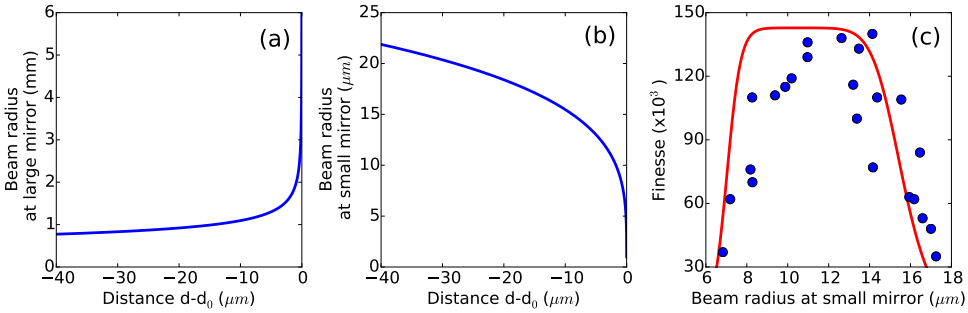

Figure 2.8: Beam radius as function of distance for (a) the mode at the large entrance mirror and (b) the mode at the small mirror of the trampoline resonator. (c) The finesse measured as function of the size of the mode at the small mirror. The red line is the expected finesse based Eqs. (2.33) and (2.34). For this measurement the diameter of the small mirror is 70 micrometer.

$d_0 = 5$ cm, the beam size at the large mirror increases rapidly, while the beam size at the small mirror decreases rapidly. The length can be set such that the beam size is small enough to fit on the trampoline resonator and not too big to clip on the large entrance mirror. These clipping losses L, both at the large and small mirror, can be modeled using the overlap between the size of the mirror and the size of the mode [36]:

$$L = 1 - \exp(-2r_{mirror}^2/w^2) \tag{2.33}$$

in which r_{mirror} is the radius of the mirror, and w the beam radius at the mirror. Together with the reflectance defined as $R = 1 - T - L$ where T is the mirror transmittance, the finesse for a high quality cavity can be written as:[10]

$$\mathcal{F} = \frac{\pi(R_1R_2)^{1/4}}{1-(R_1R_2)^{1/2}}. \tag{2.34}$$

The effect of cavity length on the finesse has been investigated experimentally by measuring the finesse via an optical ring-down together with the beam size at the small mirror. The size of the beam at the entrance mirror can be calculated using the beam size at the small mirror. With the total clipping losses calculated via Eq. (2.33), a prediction for the finesse using Eq. (2.34) is obtained. The results are shown in Fig. 2.8(c) for a trampoline resonator with mirror radius of 35 micrometer. When the beam radius at the small mirror is large, clipping losses at the small mirror reduce the finesse. For small beam sizes, obtained when the cavity length is close to d_0 (see Fig. 2.8 (b)), the dominant loss source is clipping of the beam at the large mirror. In between a flat region exists where the finesse is limited only by the coating of the mirrors.

Adjusting the cavity length carefully therefore results in the optimal finesse. Unfortunately, due to size constraints of the optical bench, the cavity length can only be adjusted by moving the entrance mirror, resulting in a misalignment of the periscope. Only via a non-trivial iterative process is the optimal alignment achieved.

2.2.4 Performing an optomechanical experiment

In section 2.1.3 we have shown how the mechanical motion can optically be reduced by using a laser with the correct detuning Δ. The laser detuning is indicated with respect to the cavity resonance. The cavity resonance frequency and laser frequency might vary over time.[11] These variations are eliminated by actively keeping track of the cavity resonance. For this the Pound-Drever-Hall (PDH) method is used [37, 38]. This is a phase sensitive detection method to keep an oscillator (laser), locked to a resonator (cavity). There are other phase sensitive methods such as homodyne detection, in which an additional laser beam serves as a phase reference. This, however,

[10] Finesse is related to optical linewidth via $\mathcal{F} = \frac{FSR}{\kappa}$, where FSR is the free spectral range of the cavity. The cavity used in this work has an FSR of 3 GHz.

[11] In practice two types of variations play a role: fast, small scale variations caused by vibrations of the set-up from external influences and slow drift in environmental temperature. To highlight the sensitivity of the set-up: when at room temperature, if the temperature changes by 1 mK, the cavity resonance frequency changes by 5 MHz, many times the optical linewidth ($\sim$ 100 kHz) of the cavity.

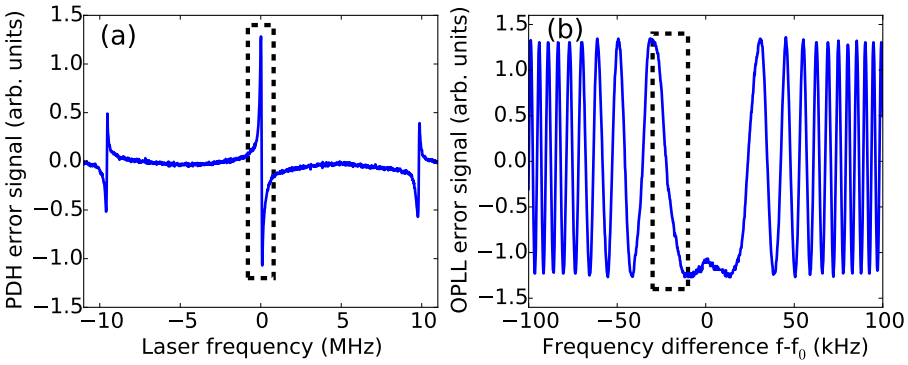

Figure 2.9: (a) PDH open-loop error signal generated by scanning the laser across a cavity resonance. (b) Open-loop error signal of the optical phase-locked loop generated by scanning the frequency of one laser while the other laser is free-running. The x-axis displays the difference frequency f-f_0 between the two lasers where f_0=3 GHz. The dashed box in both figures indicate the linear region used for the feedback.

requires that the beat signal between transmitted light and the additional laser can be measured, which is not possible for our experimental set-up.

In the case of PDH, one carrier and two sidebands created via phase modulation, are sent to the cavity. Any cavity length change will directly cause a change in phase of the resonant carrier (see Fig. 2.4(b)), while the off-resonant side-bands are directly reflected. These side-bands serve as a phase reference when measuring the interference between carrier and side-bands. In this way, any cavity length changes (or laser frequency changes) can be measured, including the motion of the trampoline resonator.

The resulting PDH signal can be used as the error signal for a PID controller to keep the laser on resonance with the cavity. An example of the open-loop error signal is shown in Fig. 2.9(a). The PDH method, therefore, serves two purposes in our experiment: the error signal provides a reference and is used for the read-out of the mechanical motion. This is only possible when the frequency of the trampoline resonator is much higher than the feedback bandwidth. If the mechanical resonance frequency falls within the feedback bandwidth, the motion of the resonator will be visible in the output of the PID controller.

In addition to a read-out laser, another laser is used to generate the optical force. Technically, the same laser can be used to generate the optical force as well, but to avoid any unwanted interference it is easier to use a second laser (when available). This second laser operates one free spectral range (FSR) of the cavity ($\sim$ 3 GHz) away from the first laser, again to avoid unwanted interference. Any drift in laser frequency is resolved by having the second laser follow the first laser via an optical phase-locked loop (OPPL), which works exactly like a normal phase-locked loop. The beat signal of the two lasers is mixed with an electrical local oscillator operating

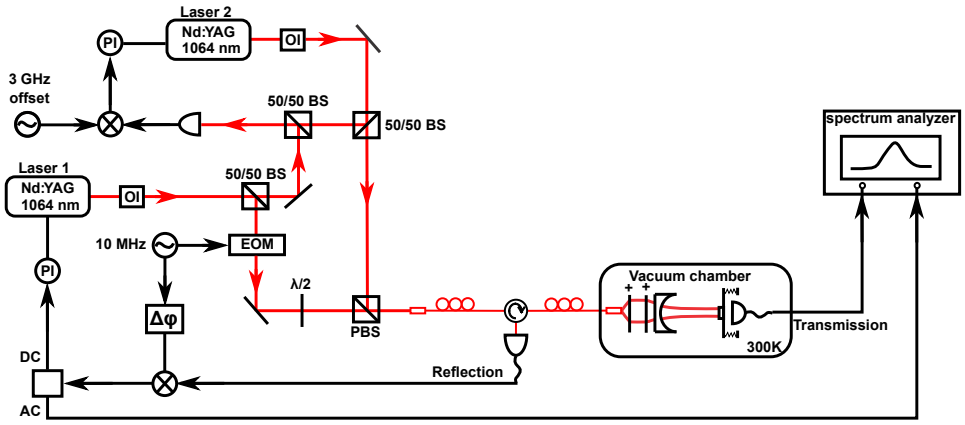

Figure 2.10: Simplified schematic of the optical set-up. The components displayed are: LO: local oscillator, BS: beam splitter, PBS: polarizing beam splitter, EOM: electro-optical modulator, OI: optical isolator and PI: proportional-integral feedback controller.

at approximately the FSR of 3 GHz.[12] The output of the mixer is shown in Fig. 2.9(b). The dashed box indicates the linear region which can be used as an error signal for a feedback loop to keep the phase of the beat signal constant with respect to the local oscillator. If we would like to change the detuning of the second laser, we change the local oscillator frequency. The frequency of the second laser is then, via a PID controller, adjusted to keep the phase of the beat the same as the phase of the local oscillator.

After alignment of the optical bench and placing the whole set-up either in a vacuum chamber or a cryostat, an optomechanical experiment begins by locking the first laser via the PDH method to a cavity resonance to provide both the reference and the read-out of the mechanical motion. Next, the second laser is locked to the first laser via the OPPL. Finally, the detuning is adjusted to see, for example, optical cooling by monitoring the mechanical power spectral density.

In Fig. 2.10 a simplified schematic is shown of the optical set-up and we will give a quick run through of the set-up and components. Laser 1 (Coherent Mephisto S) is sent through an electro-optical modulator (EOM) to generate the two sidebands needed for the PDH scheme. The light reflected from the cavity is, via a fiber circulator, picked up with a photodiode. The electrical signal is mixed with the local oscillator (LO) at 10 MHz that also drives the EOM. The low-frequency part is routed to a PI controller (VU lock-box with $\sim$30 kHz bandwidth) to lock the frequency of laser 1 to a cavity resonance. The high-frequency part is sent to a spectrum analyzer (Zurich Instruments HF2LI) to record the mechanical thermal noise spectrum S_{xx} of the mechanical resonator. To lock laser 2 (Coherent Mephisto) with a variable frequency difference to laser 1 via an OPLL, the beat signal of laser 1 and 2 is continuously monitored using a fast PIN diode (EOT ET-3500F). This signal is mixed with

[12] Alternatively, a frequency divider can be used when an appropriate frequency generator is not available. Using a divider will, however, reduce the phase stability of the OPLL.

a local oscillator around 3 GHz (Rohde and Schwarz SMA100A) to provide the error signal for the OPLL, which is directed to a fast PI-controller (VU lock-box with $\sim$30 kHz bandwidth). By adjusting the frequency of the OPLL LO, laser 2 can be set to a specific cavity detuning.

The frequency tunable range of the lasers via the piezos is limited to approximately 10 MHz. However, both lasers are also temperature tunable over a broader frequency range ($\sim$1 GHz), although with $<$1 Hz bandwidth. Therefore a slow laser frequency feedback loop for each laser is implemented based on temperature control that enables measurements for many hours with a fully automated measurement protocol.